We are IntechOpen,
the world's leading publisher of
Open Access books
Built by scientists, for scientists

4,800
Open access books available

122,000
International authors and editors

135M
Downloads

Our authors are among the

154
Countries delivered to

TOP 1%
most cited scientists

12.2%
Contributors from top 500 universities

CLARIVATE ANALYTICS

BOOK CITATION INDEX

INDEXED

WEB OF SCIENCE™

Selection of our books indexed in the Book Citation Index
in Web of Science™ Core Collection (BKCI)

Interested in publishing with us?
Contact book.department@intechopen.com

Numbers displayed above are based on latest data collected.
For more information visit www.intechopen.com

Opto-Acoustic Technique for Residual Stress Analysis

Sanichiro Yoshida and Tomohiro Sasaki

Abstract

Residual stress analysis based on co-application of acoustic and optical techniques is discussed. Residual stress analysis is a long-standing and challenging problem in many fields of engineering. The fundamental complexity of the problem lies in the fact that a residual stress is locked into the material and therefore hidden inside the specimen. Thus, direct measurement of residual stress in a completely nondestructive fashion is especially difficult. One possible solution is to estimate residual stress from the change in the elastic constant of the material. Residual stress alters the interatomic distance significantly large that the elastic constant is considerably different from the nominal value. From the change in the elastic constant and knowledge of the interatomic potential, it is possible to estimate the residual stress. This acoustic technique (acoustoelasticity) evaluates the elastic modulus of the specimen via acoustic velocity measurement. It is capable of determining the elastic modulus absolutely, but it is a single-point measurement. The optical technique (electronic speckle pattern interferometry, ESPI) yields full-field, two-dimensional strain maps, but it requires an external load to the specimen. Co-application of the two techniques compensates each other's shortfalls.

Keywords: acoustoelasticity, electronic speckle pattern interferometry, scanning acoustic microscopy, finite element modeling of residual stress, nondestructive residual stress analysis, heat-induced residual stress

1. Introduction

It is widely known that residual stresses are created by almost every material process and harmful to a variety of structures and devices [1]. Yet, the problem is far from being solved. Although a number of techniques have been developed to evaluate residual stresses, destructively [2–6] or nondestructively [7–20], have been developed to evaluate residual stresses, there is no single method applicable to general cases for accurate evaluations. The fundamental complexity of the problem lies in the fact that residual stresses are locked into the material and therefore hidden from observance. Unless the locking mechanism is removed, the residual stress is not visible from the outside. Under such a situation, it is especially difficult to diagnose residual stresses nondestructively. Techniques classified as nondestructive methods normally use diffractometry [9, 10, 19] or acoustic probing [7, 8, 12–16]. The techniques classified as diffractometry detect the atomic rearrangement due to residual stresses from a shift in the diffraction angle using X-ray, neutron, synchrotron, or similar radiation. The techniques classified as acoustic probing detect residual stresses from the change in the acoustic impedance due to

stress-induced alternation of the elastic constant. Both are well-established methods but have limitations. Diffractometry is applicable to detection of atomic rearrangement within the penetration depth of the radiation used. Neutron and synchrotron radiations can have reasonable penetration depths of tens of mm, but a large facility is required, and access is most often an issue. X-ray diffraction instruments are relatively more accessible, but the typical penetration depth is in the range of tens of μm [19]. The acoustic waves can penetrate much further, but the coupling of the acoustic signal from the emitter to the specimen is sensitive. According to our experience, the conditions of the coupling medium (usually distilled water) such as the layer thickness and the total amount can affect the measurement. Slight shifts in the contact locations seem to cause a considerable change in the measurement as well. It is not clear if such changes are due to errors associated with the contact or actual spatial variation of the residual stress. In either case, the measurement is essentially pointwise, and therefore these methods are time-consuming if applied to a certain area of the object. These issues are especially significant for analysis of welding-induced residual stress because by nature compressive and tensile residual stresses can alternate with high spatial frequency.

Given the above situation, our approach is to employ multiple methods. We are especially interested in combining an optical technique capable of full-field analysis and an acoustic technique. It should be noted that the optical methods, including the diffractometry discussed above, measure a change in displacement (strain), whereas the acoustic methods detect a change in elastic constant. With an appropriate combination of optical and acoustic techniques, we can essentially obtain both elastic constant and strain information. In principle, through the knowledge of strain with the elastic constant, we can estimate the stress. This is contrastive to the application of diffractometry by itself. In that case, even if the method provides us with accurate strain data, the residual stress heavily depends on the elastic constant to be used. The use of the nominal value (the residual stress free value) to estimate the residual stress from the measured residual strain is somewhat contradictory. The aim of this article is to discuss the application of an optical technique known as the electronic speckle pattern interferometry and acoustic methods for assessment of residual stress induced by welding. After briefly reviewing several techniques widely used for residual stress analysis, the results of our research are presented and discussed. The presented combined method is still in the process of development. It is our intention to introduce the techniques to the readers hoping that the information is useful to them. Future directions of the research are discussed as well.

2. Techniques to evaluate residual stresses

2.1 X-ray diffractometry (XRD)

In this section the principle of X-ray diffractometry (XRD) for residual stress analysis is described briefly. A more detailed description about the technique can be found elsewhere [21]. **Figure 1a** illustrates that Bragg's law relates the angle of diffraction θ and the lattice distance as follows:

$$n\lambda = 2d \sin \theta \tag{1}$$

Here n is an integer and λ is the wavelength of the X-ray. Eq. (1) represents the condition of constructive interference that takes place when the path difference between the reflections from the top lattice plane and the second lattice plane is an
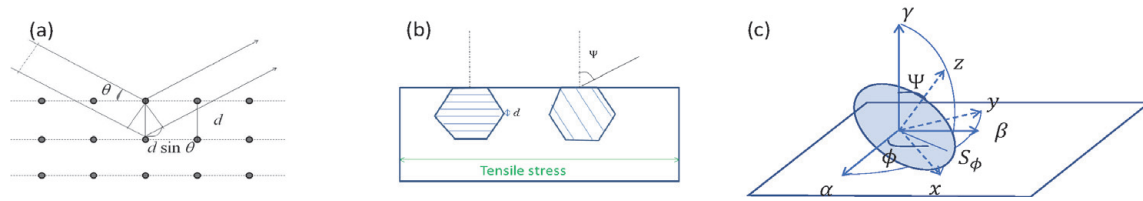
Figure 1.
(a) Bragg diffraction. (b) Change in crystallographic plane orientation and spaces due to residual stress. (c) Coordinate system αβγ affixed to specimen surface where the γ-axis is normal to specimen surface and α and β are axes of principal stress. Coordinate system xyz is affixed to grain where the z-axis is normal to lattice plane. The z-axis is rotated around the y-axis, which is in αβ-plane. S_ϕ denotes direction of in-plane strain ε_ϕ, which makes angle φ from the α-axis in αβ-plane.

integer multiple of λ. Under this condition, the detector (not shown in this figure) records a maximum when it is oriented at the angle of diffraction.

The XRD for residual stress analysis exploits the fact that an in-plane stress alters the distance between the neighboring lattice planes via Poisson's effect and thereby shifts the diffraction angle from the nominal (unstressed) value. **Figure 1b** illustrates the situation where an in-plane tensile stress increases the lattice distance in a grain whose lattice plane is oriented at angle Ψ to a line normal to the surface. The resultant change in the lattice distance $\Delta d_\Psi = d_\Psi - d_0$ from the initial distance d_0 causes the strain.

$$(\varepsilon_\Psi)_{zz} = \frac{d_\Psi - d_0}{d_0} \tag{2}$$

Here $(\varepsilon_\Psi)_{zz}$ is the normal strain along the z-axis in the coordinate system affixed to the grain, as **Figure 1c** illustrates. In this coordinate system, the lattice plane is parallel to the xy-plane and perpendicular to the z-axis. The $\alpha\beta\gamma$ coordinate system is affixed to the specimen where the γ-axis is normal to the specimen surface and α- and β-axes are the principal axes. The local stress has angle ϕ to the α-axis. Through the proper coordinate transformation, we can express this strain using the in-plane strain parallel to the specimen surface as.

$$(\varepsilon_\Psi)_{zz} = \left(\varepsilon_{\alpha\alpha} \cos^2\phi + \varepsilon_{\alpha\beta} \sin 2\phi + \varepsilon_{\beta\beta} \sin^2\phi\right) \sin^2\Psi$$
$$+\varepsilon_{\gamma\gamma} \cos^2\Psi + \varepsilon_{\gamma\alpha} \cos\phi \sin 2\Psi + \varepsilon_{\beta\gamma} \sin\phi \sin 2\Psi. \tag{3}$$

The first part on the right-hand side of Eq. (3) enclosed by the parenthesis is the in-plane strain in the direction of S_ϕ (ε_ϕ in **Figure 1**). Eq. (3) indicates that ε_ϕ is given as the slope of ε_{zz}- $\sin^2\Psi$ plot. Eq. (2) tells us the deformed lattice distance d_Ψ is proportional to ε_{zz}. These altogether indicate that the in-plane strain ε_ϕ can be given by the following differential:

$$\varepsilon_\phi = \frac{\partial(\varepsilon_\Psi)_{zz}}{\partial(\sin^2\Psi)} = \left(\varepsilon_{\alpha\alpha} \cos^2\phi + \varepsilon_{\alpha\beta} \sin 2\phi + \varepsilon_{\beta\beta} \sin^2\phi\right) \propto \frac{\partial d_\Psi}{\partial(\sin^2\Psi)}. \tag{4}$$

Since the in-plane strain ε_ϕ is connected with the in-plane stress σ_ϕ with an elastic constant, Eq. (4) indicates that σ_ϕ can be evaluated as the slope of d_Ψ vs. $\sin^2\Psi$ plot. In the present context, σ_ϕ is the in-plane residual stress of interest. Experimentally, we can evaluate σ_ϕ by changing angle Ψ and plotting the corresponding d_Ψ as a function of $\sin^2\Psi$. The deformed lattice distance d_Ψ can be determined from the corresponding shift in the diffraction angle as discussed above. When the angle Ψ is varied for this plot, the slope (4) remains unchanged.
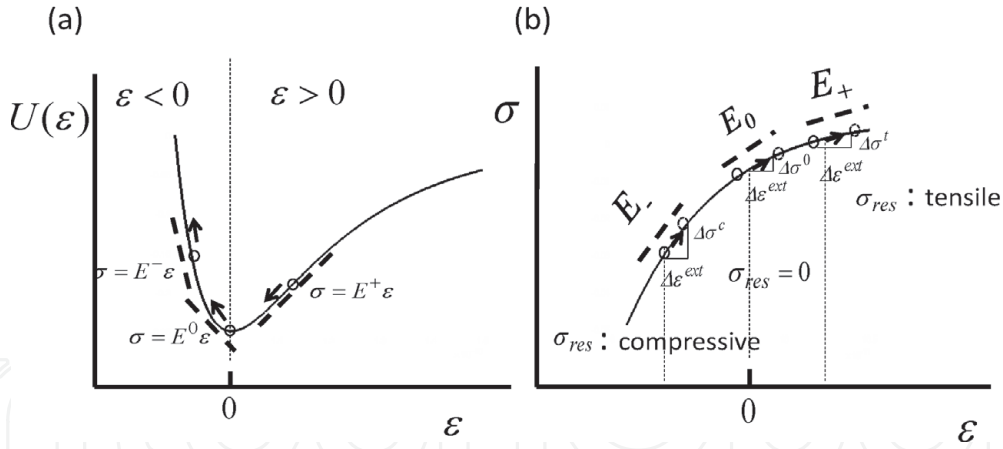
Figure 2.
(a) Interatomic potential energy curve. (b) Slope of potential energy curve.

So, d_Ψ- $\sin^2\Psi$ graph is a linear plot. Since the twice of the diffraction angle 2θ is the quantity directly measured in this type of experiment, often $2\theta - \sin^2\Psi$ graph is used to evaluate σ_ϕ. The constant of proportionality K is called the stress constant:

$$\sigma_\phi = KM \tag{5}$$

Here σ_ϕ is the residual stress, M is the slope of the $2\theta - \sin^2\Psi$ plot. K depends on the wavelength (i.e., the X-ray source line) and the lattice plane used for diffraction. As an example, for aluminum alloy 5083 with the use of Cr-Kα line for the X-ray source and the aluminum's [4 2 2] lattice plane for diffraction, $K = -168.80$ MPa/°.

2.2 Acoustoelasticity

Acoustoelasticity [14–17] evaluates residual stresses based on a change in the acoustic velocity from the nominal value. Residual stresses cause the strain so large that the elastic coefficient is altered from the nominal value. **Figure 2** illustrates the situation schematically. The strain energy curve is steeper on the short-range side of the equilibrium position (where the strain is null) than the long-range side. Consequently, the region of tensile residual stress makes the acoustic velocity lower than the nominal value, and the region of compressive residual stress makes the acoustic velocity higher. Acoustic velocity is proportional to the ratio of the elastic modulus to the density. Thus, through measurement of acoustic velocity at each point of the specimen and scanning through the entire specimen, it is possible to map out the residual stress distribution. Typically, a contact acoustic transducer is used for acoustic velocity measurement.

For quantitative analyses, the lowest order of the nonlinear terms in the elastic modulus is used. As **Figure 2** indicates, the strain energy curve is quadratic around the equilibrium (the bottom of the well). Being the first-order spatial derivative of the energy, the stress is proportional to the strain; hence, the elastic coefficient (the stress divided by the strain) is a constant. When a residual stress shifts the strain from the equilibrium, the strain energy curve is no more quadratic at that point. Hence, the elastic coefficient E becomes a function of strain and can be expressed as a polynomial expansion around the nominal value (E_0):

$$E = E_0 + C^{(3)}\varepsilon + \frac{1}{2}C^{(4)}\varepsilon^2 + \cdots + \frac{1}{(n-2)!}C^{(n)}\varepsilon^{(n-2)} + \cdots \tag{6}$$

where $C^{(n)}$ is the nth-order coefficient of the strain energy. (The exponent used for C indicates the order of the strain energy. Since the elastic constant is the slope of the strain energy, i.e., its differential, n appears on the $n-1^{th}$ term in this expression. It appears on the nth term in the potential energy expression.) Under this condition, the acoustic velocity can be expressed as follows:

$$v^{ac} = \sqrt{\frac{E_0 + C^{(3)}\varepsilon}{\rho}} \qquad (7)$$

Here ρ is the density, and up to the third order of the higher-order terms in Eq. (6) is considered. The coefficient $C^{(3)}$ is called the third-order elastic constant (TOEC). When a residual stress causes the nonlinearity, the relative acoustic velocity can be expressed with the residual strain ε_{res} and the TOEC as follows:

$$v_{rel}^{ac} = \frac{v_{res}^{ac}}{v_0^{ac}} = \sqrt{\frac{E_0 + C^{(3)}\varepsilon_{res}}{E_0}} = \sqrt{1 + \frac{C^{(3)}\varepsilon_{res}}{E_0}} \simeq 1 + \frac{1}{2}\frac{C^{(3)}\varepsilon_{res}}{E_0} \qquad (8)$$

Here v_{res}^{ac} and v_0^{ac} are the acoustic velocity in a residually stressed specimen and an unstressed specimen of the same material, respectively. By measuring these velocities and knowing the value of the TOEC, we can evaluate the residual strain by solving Eq. (8) for ε_{res} as.

$$\varepsilon_{res} = \frac{2E_0}{C^{(3)}}\left(v_{rel}^{ac} - 1\right) \qquad (9)$$

Once ε_{res} is found, the corresponding residual stress can be evaluated with the use of the nonlinear elastic modulus expression (6).

2.3 Contact acoustic transducer and scanning acoustic microscope (SAM)

A contact acoustic transducer and scanning acoustic microscope are typical devices used for the acoustoelasticity measurement.

Figure 3a illustrates a typical contact acoustic transducer arrangement. The transducer placed on the specimen surface through a coupling medium (typically distilled water) sends a pulsed longitudinal or shear acoustic wave. The signal goes
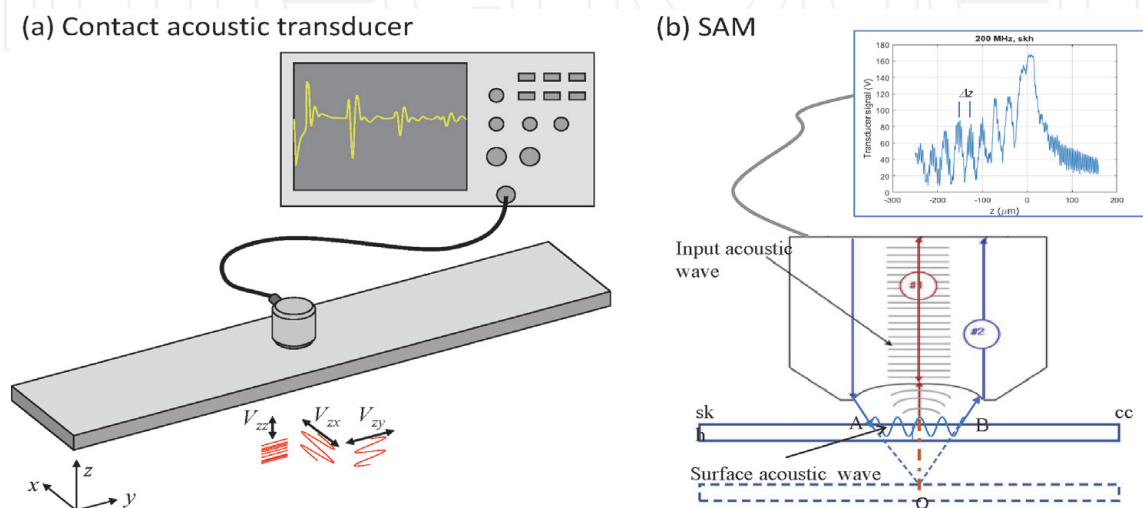
Figure 3.
(a) Typical contact acoustic transducer arrangement. (b) Working principle of SAM.

through the specimen, is reflected at the bottom surface, and returns to the trans-ducer. The received signal shows two peaks as the insert in **Figure 3a** illustrates. The first peak represents the input signal, and the second represents the returning signal. From the time of flight, the acoustic velocity inside the specimen can be evaluated for each polarization (longitudinal or shear polarization) of the acoustic signal. Since the acoustic velocity is proportional to the square root of the elastic constant for the given polarization, the elastic constant can be estimated.

Figure 3b illustrates a typical SAM setup. Details of its operation principle can be found in a number of references [22, 23]. In short, it works as follows. The acoustic lens sends the incident acoustic wave to the specimen at an angle higher than the critical angle. Consider the two acoustic paths labeled #1 and #2 in the figure. The former represents the acoustic wave incident to the specimen surface and specularly reflected off the surface. The latter represents the acoustic reradia-tion at the liquid–solid interface due to the surface acoustic wave generated by the incident wave. These two acoustic waves interfere with each other. The acoustic lens is then moved toward the specimen. As this happens, the voltage signal from the transducer (not shown in the figure) placed on top of the lens undergoes a series of crests and troughs (as the path difference goes through constructive and destructive interference). This oscillatory voltage pattern is called the V(z) curve [22]. The insert in **Figure 3b** is a sample V(z) curve. Since the frequency is fixed at the acoustic source, the acoustic path length (the path length in the unit of the wavelength) over AB depends on the phase velocity of the surface wave. Thus, the interval of these peaks (Δz) is related to the velocity of the surface acoustic wave relative to the acoustic velocity in the coupling water as follows.

$$V_s = \frac{V_w}{\sqrt{1 - \left(1 - \frac{V_w}{2\Delta z} \cdot f\right)^2}} \tag{10}$$

where V_s is the surface acoustic wave velocity, V_w is the acoustic velocity in water, and f is the acoustic frequency. The elastic modulus of the near-surface region of the specimen can be characterized from V_s:

2.4 Electronic speckle pattern interferometry (ESPI)

Figure 4a illustrates a typical electronic speckle pattern interferometry (ESPI) setup. A laser beam is split into two beams that constitute interferometric paths. The two beams are expanded and recombined on the surface of the specimen attached to the tensile machine. As superposition of coherent light beams, speckles
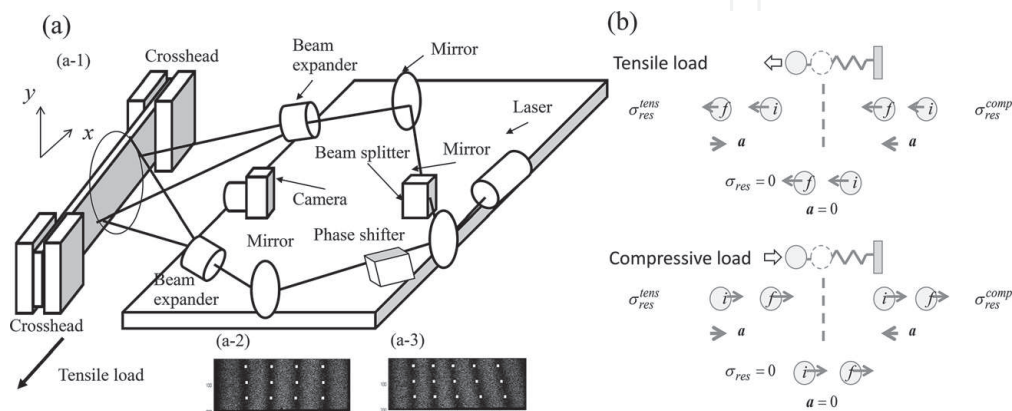
Figure 4.
(a) Typical ESPI setup. (a-1) Optical configuration. (a-2) Sample dark fringes. (a-3) Another sample dark fringes. (b) Principle of operation.

are formed in the image plane of a digital camera that captures images of the specimen. When the specimen is deformed by the tensile machine, the optical path length of one interferometric path increases and the other decreases. This changes the phase of each of all the speckles formed by the respective interfering beams. The digital camera takes images as the tensile machine keeps applying the load. The image captured at a certain time step is subtracted from the one captured at a different time step. The subtracted image exhibits an interferometric fringe pattern because the speckles undergo the phase change corresponding to the time difference between the two time steps. In those regions on the specimen where the speckles undergo a phase change corresponding to an integer multiple of 2π, the intensity of the interferometric images taken at the first and second time steps is the same. Consequently, dark fringes are formed, as illustrated by the inserts in **Figure 4a-2, a-3**.

In this arrangement the tensile machine applies a tensile load to the specimen so that the interference fringe patterns can be formed at least in three time steps. The applied load is kept as small as possible so that it does not relax the residual stress on the specimen. Since each of the fringe patterns contains the contours of displacement that the specimen undergoes in the duration between the first and second images are captured, the physical information contained by the fringe pattern represents the velocity. So, by subtracting two fringe patterns obtained by subtraction consecutively, the resultant frame contains acceleration of the points on the specimen surface. With the algorithm described below, it is possible to diagnose the status of residual stress through analysis of these frames containing the acceleration information.

Figure 4b illustrates the principle of operation. Consider that a certain part of the specimen has a compressive residual stress. As the top right part of this figure illustrates, the situation can be modeled by a mass connected to a compressed spring. If an external agent applies a tensile load (the load opposite to the compression), the mass returns to the equilibrium (represented by a dashed line in the figure) with acceleration in the same direction as the applied load. If the residual stress is tensile, the same external load displaces the mass away from the equilibrium. Hence, in this case, the acceleration of the mass is opposite to the applied load. This mechanism can be summarized as follows. "If the residual stress and applied load are of the same type (tensile or compression), the acceleration is opposite to the applied load. Otherwise, the acceleration is in the same direction as the applied load." The situation is the same when the applied load is compressive, as illustrated in the lower part of **Figure 4b**.

By applying this algorithm to diagnose the type of residual stress at a given point and combining it with the abovementioned formation of fringe pattern representing acceleration, it is possible to map out the type of residual stress on all points of the specimen.

It is also possible to estimate the elastic modulus at all points. As mentioned above, the fringe pattern resulting from subtraction of the interferometric image taken at one time step from another time step represents the displacement occurring in the time difference between the two time steps. By evaluating the displacement at all coordinate points (e.g., via interpolation between dark fringes) and dividing them by the pixel interval, it is possible to map out strain as a full-field two-dimensional data. By assuming that all the points on the specimen are under equilibrium when the tensile machine applies the load, the stress can be evaluated by dividing the applied load by the cross-sectional area of the specimen. This procedure yields a map of relative elastic modulus over the specimen. If the third-order elastic constant of the material is known, the elastic modulus can be calibrated by performing an acoustic velocity measurement at several points of the specimen.

This yields a map of absolute elastic modulus, and from this data the residual strain can be evaluated with Eq. (6).

Once the residual strain is found, the residual stress can be estimated as follows:

$$\sigma_{res} = \left(E_0 + C^{(3)} \varepsilon_{res} \right) \varepsilon_{res} \tag{11}$$

2.5 Finite element modeling (FEM)

Accurate numerical modeling of residual stress is extremely difficult. However, finite element modeling is useful because it can provide us with some insight and qualitative analysis when combined with experiment. This section discusses frameworks of such modeling in conjunction with the TOEC algorithm. For simplicity, the discussion here is limited to an isotropic case [24].

With the third-order term included, the constitutive relation can be expressed as follows:

$$
\begin{pmatrix} \sigma_1 \\ \sigma_2 \\ \sigma_3 \\ \sigma_4 \\ \sigma_5 \\ \sigma_6 \end{pmatrix} = \left\{ \begin{pmatrix} C_{11} & C_{12} & C_{13} & C_{14} & C_{15} & C_{16} \\ C_{21} & C_{22} & C_{23} & C_{24} & C_{25} & C_{26} \\ C_{31} & C_{32} & C_{33} & C_{34} & C_{35} & C_{36} \\ C_{41} & C_{42} & C_{43} & C_{44} & C_{45} & C_{46} \\ C_{51} & C_{52} & C_{53} & C_{54} & C_{55} & C_{56} \\ C_{61} & C_{62} & C_{63} & C_{64} & C_{65} & C_{66} \end{pmatrix} \right.
$$
$$
\left. + \begin{pmatrix} \Delta C_{11} & \Delta C_{12} & \Delta C_{13} & \Delta C_{14} & \Delta C_{15} & \Delta C_{16} \\ \Delta C_{21} & \Delta C_{22} & \Delta C_{23} & \Delta C_{24} & \Delta C_{25} & \Delta C_{26} \\ \Delta C_{31} & \Delta C_{32} & \Delta C_{33} & \Delta C_{34} & \Delta C_{35} & \Delta C_{36} \\ \Delta C_{41} & \Delta C_{42} & \Delta C_{43} & \Delta C_{44} & \Delta C_{45} & \Delta C_{46} \\ \Delta C_{51} & \Delta C_{52} & \Delta C_{53} & \Delta C_{54} & \Delta C_{55} & \Delta C_{56} \\ \Delta C_{61} & \Delta C_{62} & \Delta C_{63} & \Delta C_{64} & \Delta C_{65} & \Delta C_{16} \end{pmatrix} \right\} \begin{pmatrix} \varepsilon_1 \\ \varepsilon_2 \\ \varepsilon_3 \\ \varepsilon_4 \\ \varepsilon_5 \\ \varepsilon_6 \end{pmatrix} \tag{12}
$$

Here the first term inside the bracket on the right-hand side is the second-order elastic coefficient, and the second term is the third-order elastic coefficient. In the case of an isotropic material, the third-order elastic coefficient can be expressed as follows [25]:

$$
\begin{pmatrix} \Delta C_{11} \\ \Delta C_{21} \\ \Delta C_{31} \\ \Delta C_{41} \\ \Delta C_{51} \\ \Delta C_{61} \end{pmatrix} = \begin{pmatrix} C_{111} & C_{112} & C_{112} & 0 & 0 & 0 \\ C_{112} & C_{112} & C_{123} & 0 & 0 & 0 \\ C_{112} & C_{123} & C_{112} & 0 & 0 & 0 \\ 0 & 0 & 0 & C_{144} & 0 & 0 \\ 0 & 0 & 0 & 0 & C_{155} & 0 \\ 0 & 0 & 0 & 0 & 0 & C_{155} \end{pmatrix} \begin{pmatrix} \varepsilon_1 \\ \varepsilon_2 \\ \varepsilon_3 \\ \varepsilon_4 \\ \varepsilon_5 \\ \varepsilon_6 \end{pmatrix} \tag{13}
$$

$$
\begin{pmatrix} \Delta C_{12} \\ \Delta C_{22} \\ \Delta C_{32} \\ \Delta C_{42} \\ \Delta C_{52} \\ \Delta C_{62} \end{pmatrix} = \begin{pmatrix} C_{112} & C_{112} & C_{123} & 0 & 0 & 0 \\ C_{112} & C_{111} & C_{112} & 0 & 0 & 0 \\ C_{123} & C_{112} & C_{112} & 0 & 0 & 0 \\ 0 & 0 & 0 & C_{155} & 0 & 0 \\ 0 & 0 & 0 & 0 & C_{144} & 0 \\ 0 & 0 & 0 & 0 & 0 & C_{155} \end{pmatrix} \begin{pmatrix} \varepsilon_1 \\ \varepsilon_2 \\ \varepsilon_3 \\ \varepsilon_4 \\ \varepsilon_5 \\ \varepsilon_6 \end{pmatrix} \tag{14}
$$

$$
\begin{pmatrix} \Delta C_{13} \\ \Delta C_{23} \\ \Delta C_{33} \\ \Delta C_{43} \\ \Delta C_{53} \\ \Delta C_{63} \end{pmatrix} = \begin{pmatrix} C_{112} & C_{123} & C_{112} & 0 & 0 & 0 \\ C_{123} & C_{112} & C_{112} & 0 & 0 & 0 \\ C_{112} & C_{112} & C_{111} & 0 & 0 & 0 \\ 0 & 0 & 0 & C_{155} & 0 & 0 \\ 0 & 0 & 0 & 0 & C_{144} & 0 \\ 0 & 0 & 0 & 0 & 0 & C_{155} \end{pmatrix} \begin{pmatrix} \varepsilon_1 \\ \varepsilon_2 \\ \varepsilon_3 \\ \varepsilon_4 \\ \varepsilon_5 \\ \varepsilon_6 \end{pmatrix} \tag{15}
$$

$$
\begin{pmatrix} \Delta C_{14} \\ \Delta C_{24} \\ \Delta C_{34} \\ \Delta C_{44} \\ \Delta C_{54} \\ \Delta C_{64} \end{pmatrix} = \begin{pmatrix} 0 & 0 & 0 & C_{144} & 0 & 0 \\ 0 & 0 & 0 & C_{155} & 0 & 0 \\ 0 & 0 & 0 & C_{155} & 0 & 0 \\ C_{144} & C_{155} & C_{155} & 0 & 0 & 0 \\ 0 & 0 & 0 & 0 & 0 & C_{456} \\ 0 & 0 & 0 & 0 & C_{456} & 0 \end{pmatrix} \begin{pmatrix} \varepsilon_1 \\ \varepsilon_2 \\ \varepsilon_3 \\ \varepsilon_4 \\ \varepsilon_5 \\ \varepsilon_6 \end{pmatrix} \tag{16}
$$

$$
\begin{pmatrix} \Delta C_{15} \\ \Delta C_{25} \\ \Delta C_{35} \\ \Delta C_{45} \\ \Delta C_{55} \\ \Delta C_{65} \end{pmatrix} = \begin{pmatrix} 0 & 0 & 0 & 0 & C_{155} & 0 \\ 0 & 0 & 0 & 0 & C_{144} & 0 \\ 0 & 0 & 0 & 0 & C_{155} & 0 \\ 0 & 0 & 0 & 0 & 0 & C_{456} \\ C_{155} & C_{144} & C_{155} & 0 & 0 & 0 \\ 0 & 0 & 0 & C_{456} & 0 & 0 \end{pmatrix} \begin{pmatrix} \varepsilon_1 \\ \varepsilon_2 \\ \varepsilon_3 \\ \varepsilon_4 \\ \varepsilon_5 \\ \varepsilon_6 \end{pmatrix} \tag{17}
$$

$$
\begin{pmatrix} \Delta C_{16} \\ \Delta C_{26} \\ \Delta C_{36} \\ \Delta C_{46} \\ \Delta C_{56} \\ \Delta C_{66} \end{pmatrix} = \begin{pmatrix} 0 & 0 & 0 & 0 & 0 & C_{144} \\ 0 & 0 & 0 & 0 & 0 & C_{155} \\ 0 & 0 & 0 & 0 & 0 & C_{155} \\ 0 & 0 & 0 & 0 & C_{456} & 0 \\ 0 & 0 & 0 & C_{456} & 0 & 0 \\ C_{155} & C_{155} & C_{144} & 0 & 0 & 0 \end{pmatrix} \begin{pmatrix} \varepsilon_1 \\ \varepsilon_2 \\ \varepsilon_3 \\ \varepsilon_4 \\ \varepsilon_5 \\ \varepsilon_6 \end{pmatrix} \tag{18}
$$

The isotropic TOE tensor is described by three linearly independent elements [24]. Choosing C_{123}, C_{144}, and C_{456} to be the three independent elements, we can use the following relations for complete expression of the third-order coefficient:

$$
C_{111} = C_{123} + 6C_{144} + 8C_{456} \tag{19}
$$

$$
C_{112} = C_{123} + 2C_{144} \tag{20}
$$

$$
C_{155} = C_{144} + 2C_{456} \tag{21}
$$

By substituting Eqs. (19)–(21) into Eqs. (13)–(18), we can find the third-order effect for each stress tensor component.

To compare with acoustoelastic measurement, it is necessary to express the effect of the inclusion of the third-order elastic coefficient in the corresponding acoustic velocity. Assuming that the density is unaffected by the inclusion of the third-order effect, the relative acoustic velocity can be expressed as follows:

$$\frac{v_{ij}^{(3)}}{v_{ij}^{(2)}} = \frac{\sqrt{(c_{ij} + \Delta C_{ij})/\rho}}{\sqrt{C_{ij}/\rho}} = \sqrt{\frac{(c_{ij+\Delta C_{ij}})}{C_{ij}}} \tag{22}$$

Here $i, j = 1 \ldots 6$, and $v_{ij}^{(3)}$ and $v_{ij}^{(2)}$ denote the acoustic velocity of the corresponding mode with and without the third-order effect.

3. Experimental observations and numerical analysis

3.1 Carbon steel and cemented carbide dissimilar welding

As an example of dissimilar welding, we discuss here a previous analysis [26] on butt-brazing of a carbon steel (skh51) and cemented carbide (V30). **Figure 5a** illustrates the arrangement of the brazing. An skh51 plate of 18.5 mm wide, 50 mm long, and 3.37 mm thick was placed on a mount with the 18.5 mm side contacting a V30 plate of the same dimension. For approximately 30 mm in length around the contacting area, an induction coil was arranged to heat the specimen for brazing. On brazing, Ag braze paste (Ag-Cu-Zn-Ni alloy, ISO Ag450) was put on the contact surface, and a braze temperature of 800°C was applied for 10 s. After this 10 s period, the brazed specimen was air-cooled. The noncontacting 18.5 mm sides of the respective plates were clamped to the steel blocks as shown in **Figure 5a**. The two steel blocks were connected via slide guides for free vertical slide. This means that the only constrain on the plates during the brazing operation was gravity. **Table 1** shows the material constants of skh51 and V30.

A contact acoustic transducer and a scanning acoustic microscope (SAM) were used for the analysis. The acoustic signal from the contact acoustic transducer travels through the entire thickness of the specimen. Thus, the measured acoustic velocity indicates the elastic property averaged over the specimen thickness. On the
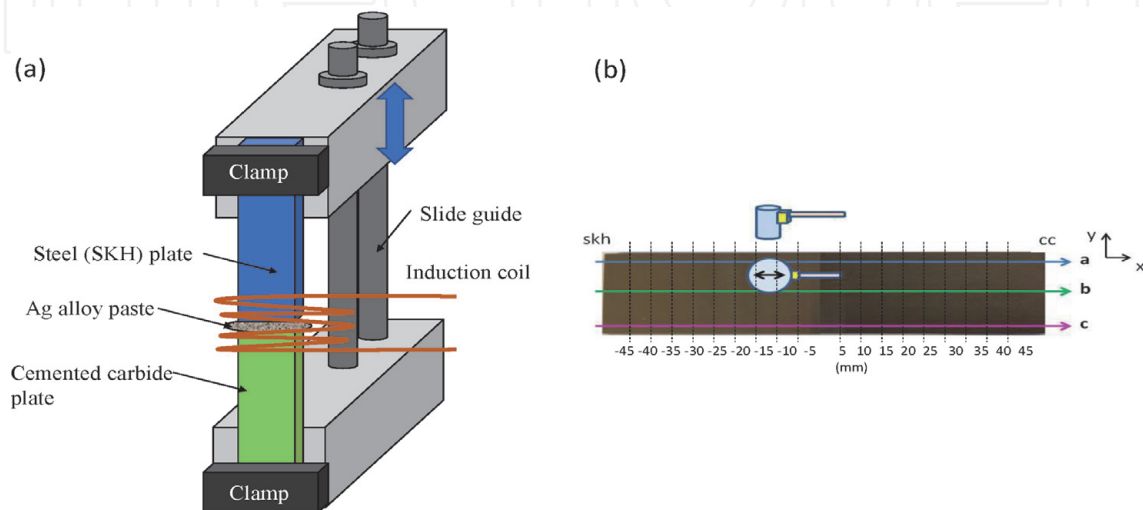
Figure 5.
(a) Setup for skh-cc welding (brazing). (b) Butt-brazed specimen and coordinate points for acoustic measurements.

Material	Steel (skh51)	Cemented carbide (V30)
Elastic modulus (GPa)	219	580
Thermal expansion (10^{-6} K^{-1})	11.9	5.3
Thermal conductivity (W m $^{-1}$ K^{-1})	23.0	67.0

Table 1.
Material constants of the brazed plates.
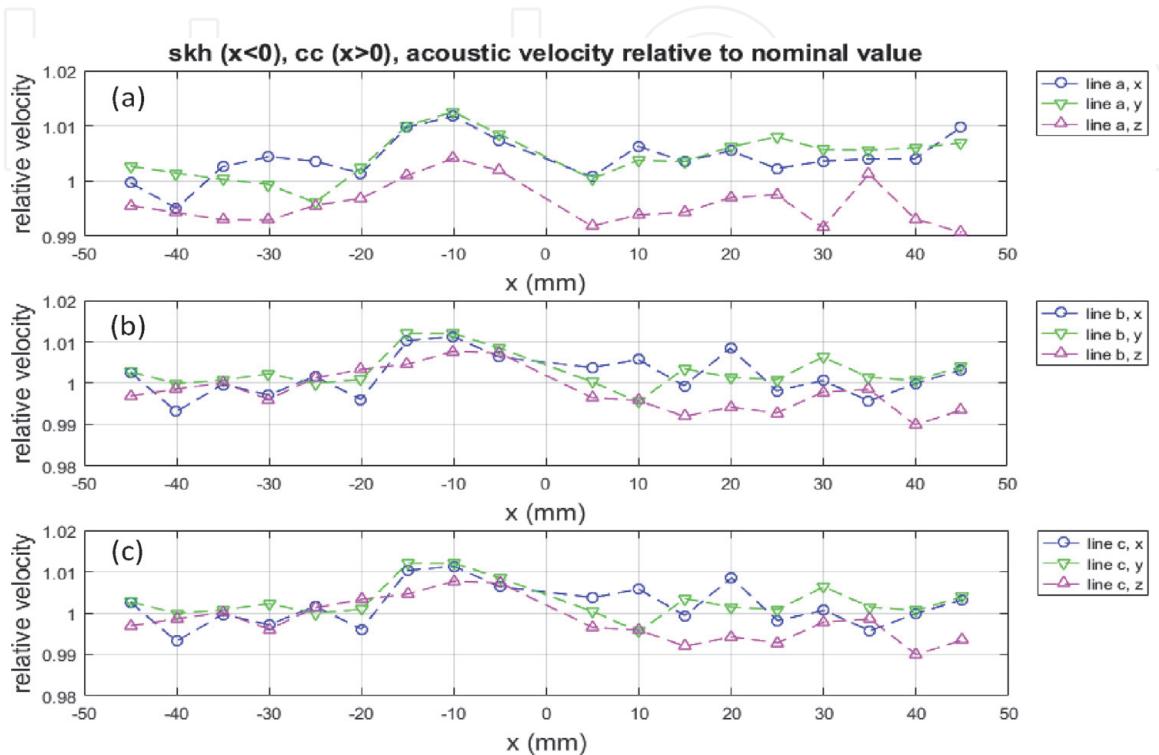
Figure 6.
Acoustic velocities relative to nominal value. (a) Line a, (b) line b, and (c) line c.

other hand, the acoustic signal emitted from the transducer head of the SAM is focused in a subsurface area of the specimen. Therefore, it detects the elastic property of the subsurface region. Hence, through a comparison of data from the contact acoustic transducer and the SAM, we can obtain information regarding the depth of the residual stress.

Figure 5b shows the butt-brazed specimen and the coordinate points where the acoustic measurements were conducted. The shear wave and longitudinal wave velocities were measured with contact acoustic transducers (Olympus V156-RM and M110-RM, respectively), driven commonly by a square wave pulser/receiver (Model 5077PR). The surface acoustic wave velocity was measured with a SAM (Olympus UH3) with 200 and 400 MHz transducer heads in the burst mode for V(z) curve analysis [22, 23].

3.2 Transverse residual stress profile

Figure 6 plots the acoustic velocities relative to the nominal values (measured before the brazing). Here the three graphs are for reference line a, line b, and line c (labeled in **Figure 5b**) from top to bottom. The following observations can be made.

3.2.1 Observation 1

The longitudinal wave (z-wave) velocity shows the following features. On the V30 side, it is lower than the nominal value for the entire horizontal span

($0 < x < 50$ mm). On the skh51 side, the velocity is clearly higher than the nominal value in the near-joint region ($-20 < x < 0$ mm) and slightly lower than the nominal value toward the cold end ($x < -20$ mm). These features can be translated into the following characteristics in the residual stress in the z-direction. The V30 side experiences tensile stress uniformly over the entire horizontal span. The skh51 side experiences compressive residual stress near the joint and very slight tensile stress for the rest of the horizontal span. Along reference line a, the situation toward the cold end on the skh51 side is slightly different. The material experiences clearer tensile residual stress.

3.2.2 Observation 2

The shear wave velocities (commonly for the x- and y-waves) show the following features. On the V30 side, the velocity is slightly higher than the nominal value for the entire horizontal span. On the skh51 side, the velocities are clearly higher than the nominal values in the near-joint region ($-20 < x < 0$ mm) and approximately the same as the nominal value for the rest of the region. These features indicate the following characteristics in the in-plane residual stresses. The V30 side experiences slight compressive residual stress uniformly over the horizontal span. On the skh51 side, the near-joint region experiences compressive residual stress. In the region toward the cold end, the material experiences tensile residual stress at a low level around reference lines b and c. Around reference line a, the residual stress in the x-direction is considerably compressive.

The above observations indicate the following overall residual stresses. On the V30 side, the residual stress is tensile along the thickness and slightly compressive along the surface plane. In both cases, the residual stress is uniformly distributed over the entire horizontal span. On the skh51 side, the residual stress is concentrated in the near-joint region where the residual stress is compressive in all directions. Toward the cold end, the residual stress is slightly tensile in all directions around reference lines b and c. Near reference line a, the residual stress is more tensile in the z-direction and compressive in the x-direction.

Possible explanations of these features found in the residual stresses are as follows:

1. The more uniform feature observed on the V30 side is due to the higher thermal conductivity (**Table 1**). The heat input from the joint flows relatively easily to the cold end on the V30 side. Consequently, the thermal effect is uniform on this size. Contrastively, due to the poor thermal conductivity, the heat input is confined in the near-joint region $-20 < x < 0$ mm (called the heat-affected zone, HAZ) on the skh51 side.

2. The compressive residual stress in the HAZ of skh51 ($-20 < x < 0$ mm) results from the following effects. In the heating phase, the HAZ experiences body-centered cubic (bcc) to face-centered cubic (fcc) phase transformation. This process is accompanied by an increase in the density. Consequently, the thermal expansion of the HAZ is smaller as compared with the non-heat-affected zone (the non-HAZ) in the $-50 < x < -20$ mm region. In the cooling phase, the HAZ of skh51 experiences fcc to bcc phase transformation. Consequently, it undergoes relatively smaller shrinkage.

3. The above phenomena affect the HAZ of the skh51side differently along the x-axis than the y- and z-axes. Along the x-axis, the following events take place. In the heating phase, the HAZ is compressed by the non-HAZ of the skh51 side and the V30 side. The non-HAZ undergoes larger thermal expansion because
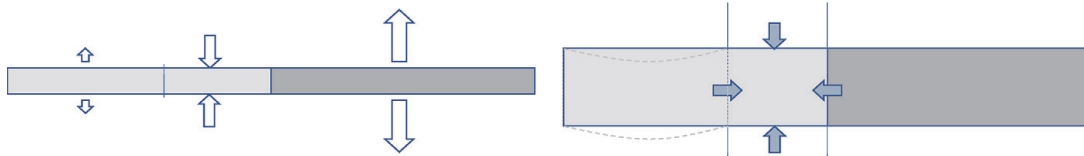
Figure 7.
Deformation induced by thermal load due to brazing and other constraints. Inward arrows represent compressive residual stress and outward arrows tensile residual stress. Sizes of arrows represent the magnitude of residual stress.

the phase transformation does not take place. The V30 side experiences uniform thermal expansion with the cool end constrained by the table of the welding setup. The gravity acts in favor of this compression experienced by the HAZ. The greater elastic modulus of V30 also helps this compressing mechanism. In the cooling phase, the HAZ of skh51 shrinks less than the other regions (the non-HAZ of skh51 and the V30 side). This makes the HAZ of skh51 tend to be stretched by the other regions. However, this time the stretching force is against the gravity. Consequently, the compressive stress formed in the heating phase remains in the HAZ on the skh51 side.

4. The events along the y- and z-axes are slightly different. At the boundary (the joint), the higher thermal conductivity makes the expansion (in the heating phase) and shrinkage (in the cooling phase) faster on the V30 side than the skh51 side. Consequently, when the skh51 side is still shrinking, the V30 side has already completed the shrinkage, preventing the skh51 side from further shrinkage. Consequently, the skh51 side is compressed along the y- and z-axes at the boundary.

5. The residual stress on the V30 side results from the above events. As the reaction to the compressive stress on the skh51 in the cooling phase, the V30 side experiences tensile stress in the y and z-directions at the boundary. Between these two directions, the material is less constrained in the z-direction due to the shorter span of the joint. Along the x-axis, the V30 side is constrained by the skh51 at the joint and by the table at the cool end. Consequently, it is likely that the tensile deformation occurs preferably in the z-direction. By Poisson's effect, the material on the V30 side undergoes compressive deformation in the x and y-directions. This explains the observation of relative acoustic velocity greater than unity in these directions on the V30 side.

6. The different behavior observed on the skh51 side along reference line a from reference lines b and c is due to the involvement of rotational displacement at the boundary. When the V30 side exerts compressive force in the x-direction on the skh51 side at the joint, the force induces counterclockwise rotation around the z-axis (in **Figure 5b**). This causes the compressive stress on the reference line a side of the specimen.

**Figure 7** illustrates this observation schematically with some exaggeration.

4. Depth of residual stress

Another important factor in residual stress analysis in general is the information regarding the depth of residual stresses. The capability to detect the depth of

residual stresses is important not only to identify the depth of a given residual stress accurately but also to prevent the possibility to overlook residual stresses. The X-ray diffractometry (XRD) is one of the most developed methods of residual stress analysis. However, the XRD is applicable to the identification of residual stresses within the penetration depth of the X-ray, which is typically a few hundreds of μm from the surface.

One way to evaluate the depth of residual stresses is to apply a contact acoustic transducer and SAM to the same specimen. In the experiment discussed here [27], the following configurations are used for the acoustic devices: (i) the SAM (Olympus UH3) with a 400 MHz transducer head and a spherical lens (310 μm focal length); (ii) the SAM with a 200 MHz transducer head and the same spherical lens as (ii); (iii) the SAM with a 200 MHz transducer head and a cylindrical lens of the same focal length (310 μm) as the spherical lens; (iv) the contact acoustic transducer with a longitudinal wave sensor head (M110-RM); and (iv) the contact acoustic transducer with a shear wave sensor head (V156-RM). These configurations work differently as follows. The SAM generates a Rayleigh wave [28] on the surface of the specimen [23]. The Rayleigh wave is mostly out of plane (normal to the specimen surface) but contains in-plane components (the component whose acoustic oscillation is parallel to the surface). When the incident acoustic wave is focused with a spherical lens, a surface acoustic wave is generated in random directions parallel to the specimen surface. Consequently, the in-plane components are averaged out, and the resultant (superposed) acoustic oscillation is out of plane. So, signals with configurations (i), (ii), and (iv) are sensitive to the elastic modulus in the z-direction. When the same incident wave from the SAM is line-focused with a cylindrical lens, on the other hand, the in-plane components whose acoustic oscillation is perpendicular to the axis of the cylindrical lens are not averaged out. Thus, the resultant acoustic wave is sensitive to the elastic modulus in the direction perpendicular to the lens's axis. So, signals with configurations (ii) and (v) are sensitive to the elastic modulus in the x or y direction (depending on the orientation of the cylindrical lens and the shear wave sensor head).

Figure 8 compares the measurement conducted with configurations (i) SAM 400 MHz spherical lens, (ii) SAM 200 MHz spherical lens, and (iv) contact acoustic transducer with the longitudinal wave mode. The 400 MHz SAM and 200 MHz SAM used the same acoustic spherical lens (310 μm focal length). Hence, the angle of incidence of the acoustic wave to the specimen surface was the same. The penetration depth of the acoustic wave is of the order of the acoustic wave length, i.e., approximately 15 μm for skh51 and 17 μm for V30. The longitudinal bulk acoustic wave from the contact transducer passes through the specimen and reflects off the rear surface. Therefore, the acoustic velocity data represents the elastic
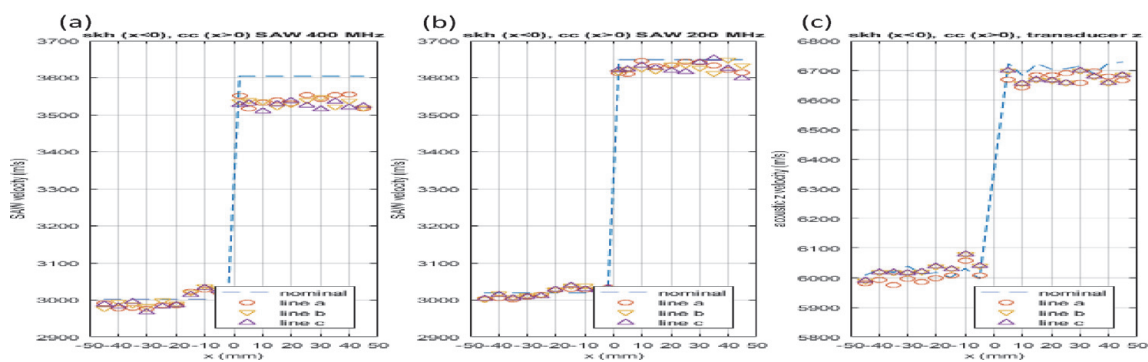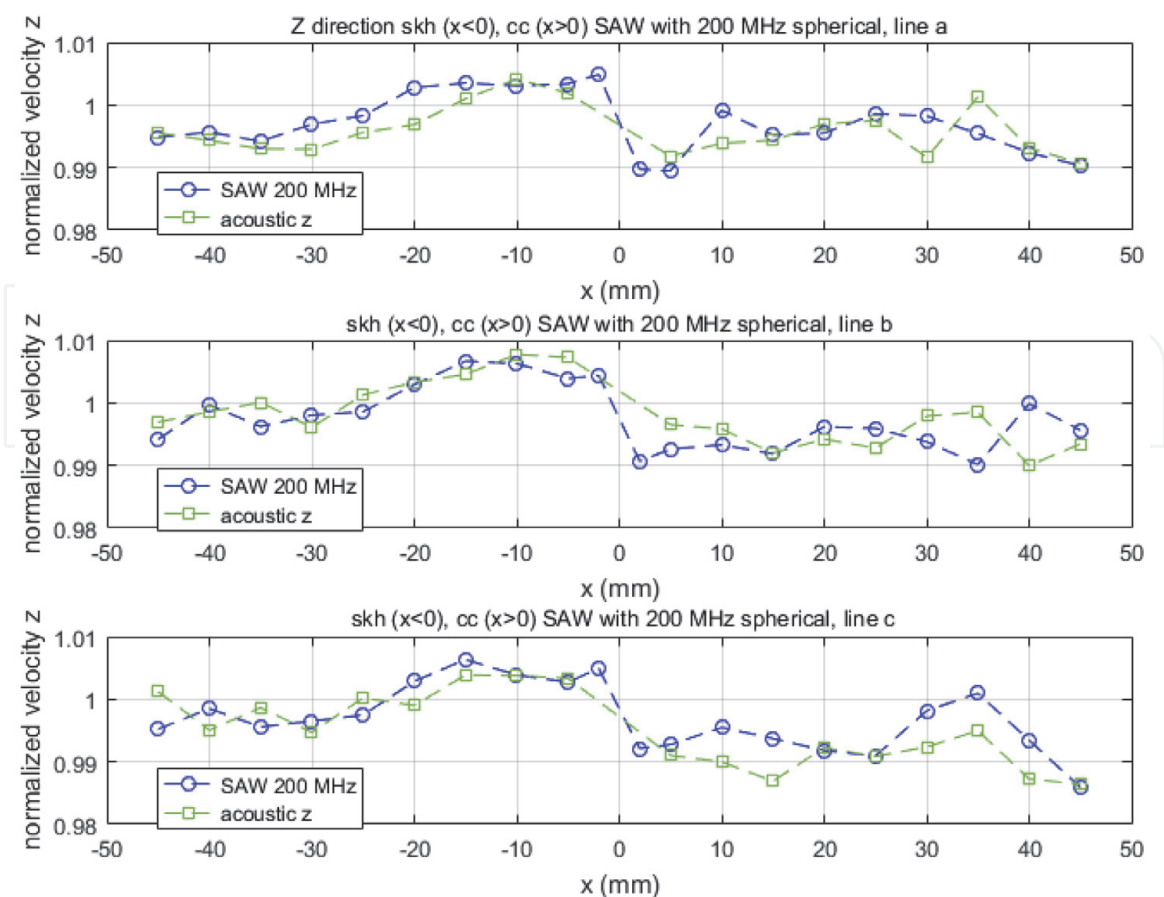

Figure 8.
Comparison of acoustic velocity data obtained with (a) SAM with 400 MHz head, (b) SAM with 200 MHz head, and (c) contact acoustic transducer.

modulus averaged over the entire thickness. The acoustic velocity data with 400 MHz SAM shows much greater deviation in the acoustic velocity from the nominal value than the 200 MHz SAM or the contact transducer. On the other hand, the data with (ii) the 200 MHz SAM and (iv) the contact transducer with the longitudinal mode are similar to each other. **Figure 9** shows the similarity between (ii) and (iv) more clearly by expressing the signal and the relative velocity to the nominal value. These indicate that the residual stress in this specimen is localized within approximately 20 μm from the surface.

While the longitudinal wave data taken with the contact acoustic transducer is similar to the SAM data with 200 MHz, the shear wave data obtained with (v) the contact acoustic transducer shows considerable difference from the data taken with (iii) the 200 MHz SAM with the cylindrical lens of the same focal length (310 μm focal length) as the spherical lens. **Figure 10** compares the data between the contact acoustic transducer and SAM for the oscillation direction of x and y, respectively. In both directions, the signal from the SAM shows considerable difference from the bulk shear wave from the contact acoustic transducer on the V30 side, while no difference is seen on the skh51 side. This indicates that on the V30 side, the material undergoes significant in-plane tensile deformation at the region twice as deep as the out-of-plane expansion (the wavelength at 200 MHz is twice of that at 400 MHz).

Comparison was also made between the optical interferometric data and acoustic data. **Figure 11** compares the acceleration map obtained by the ESPI and relative acoustic velocity (shear wave with oscillation along x). Qualitative agreement is seen indicating the consistency between the stress evaluation based on the acceleration algorithm and the acoustoelasticity.
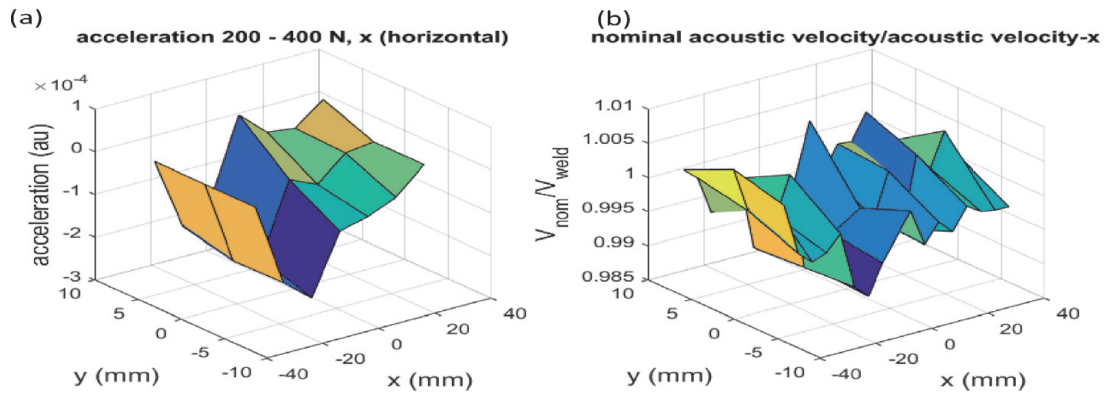

Figure 9.
*Comparison of SAM with 200 MHz head data and contact acoustic transducer.*
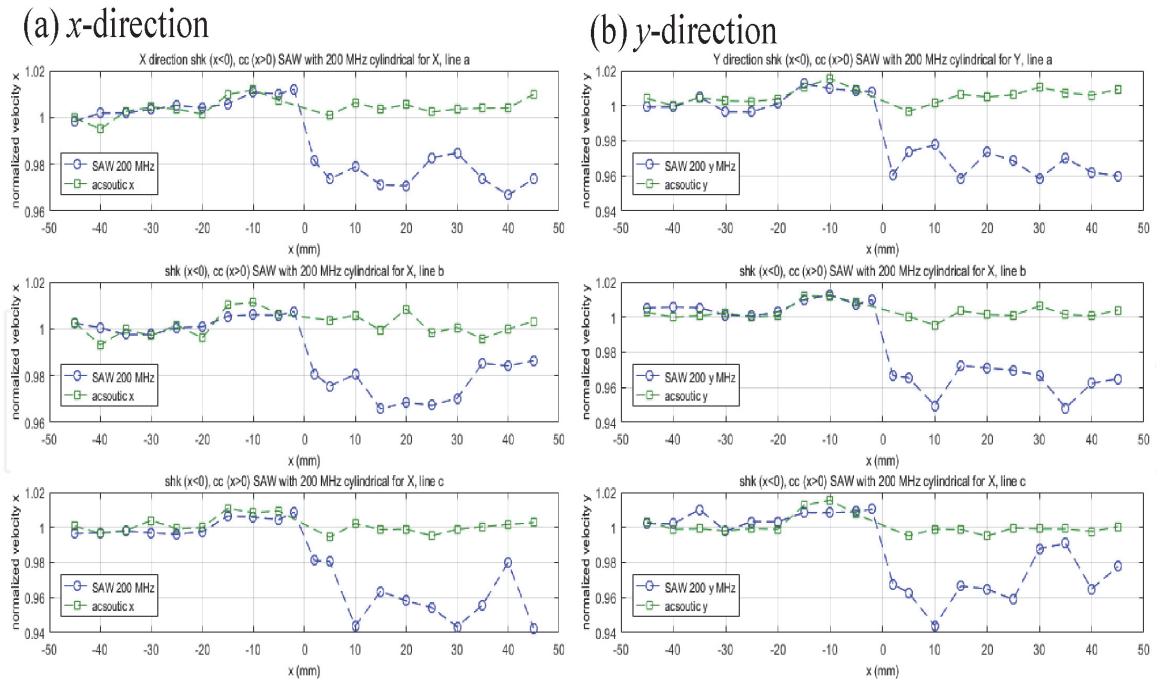
Figure 10.
Comparison of shear wave velocity obtained with contact acoustic transducer and SAM with 200 MHz shear mode transducer head.

Figure 11.
Comparison of ESPI acceleration (x) and acoustic velocity (x). (a) ESPI, and (b) Acoustic transducer x.

4.1 Bead-on-plate welding on Al 5083

A similar analysis was made for an aluminum alloy specimen [29]. The specimen used in this experiment was a bead-on-plate aluminum alloy 5083 [30] processed by gas tungsten arc (TIG) welding. **Figure 12** shows a photo of the specimen and the steel block used to place the specimen for welding. **Table 2** lists the welding condition. The specimen plate was placed on a steel block that held one end of the specimen without imposing any other constraint. The TIG welding torch applied
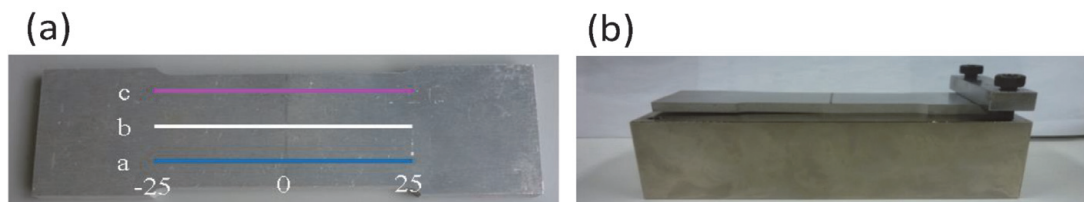
Figure 12.
(a) Al 5083 bead-on-plate specimen. Acoustic measurements were made along line a-c. (b) Specimen placed on steel block for welding.

Welding speed	Welding current	Welding voltage	Shielding gas	Cooling
5.0 mm/s	100 A	200 V	Ar (10 l/min)	Ambient air

Table 2.
Bead-on-plate welding condition.

the heat on the top surface of the specimen from the bottom end (the side close to reference line a in **Figure 12**) toward the top end (the side close to line c). During the heating process and the postheating phase, the specimen was air-cooled.

5. Acoustic, optical, and XRD measurements

For the Al 5083 specimen, the same type of acoustic and optical measurement as the skh51-V30 dissimilar weld specimen was made. The same contact acoustic transducer was used at the same coordinate points for the acoustic wave velocity measurement, and the same ESPI setup was used for the acceleration measurement. In addition, XRD analysis based on the 2θ-$\sin^2\Psi$ plot and FEM analysis were conducted. The FEM model simulated the TIG welding by a Gaussian profiled heat input (1.2 cm full width at half maximum) moving at the speed of the welding torch with an electric power of 20 kW and a coupling coefficient to the specimen of 0.9%. The cooling phase (500 s) was simulated with natural convection at all the surfaces. The deformation was made permanent when the strain exceeded a preset yield strain. More about this modeling can be found in [29]. **Figure 13** compares the results from the above four types of analyses. The data is presented in the form of two-dimensional mapping where the vertical axis represents a physical quantity associated with the residual stress in the x-direction. The ESPI analysis presents the acceleration in the x-direction, the XRD and FEM analyses present x-component of
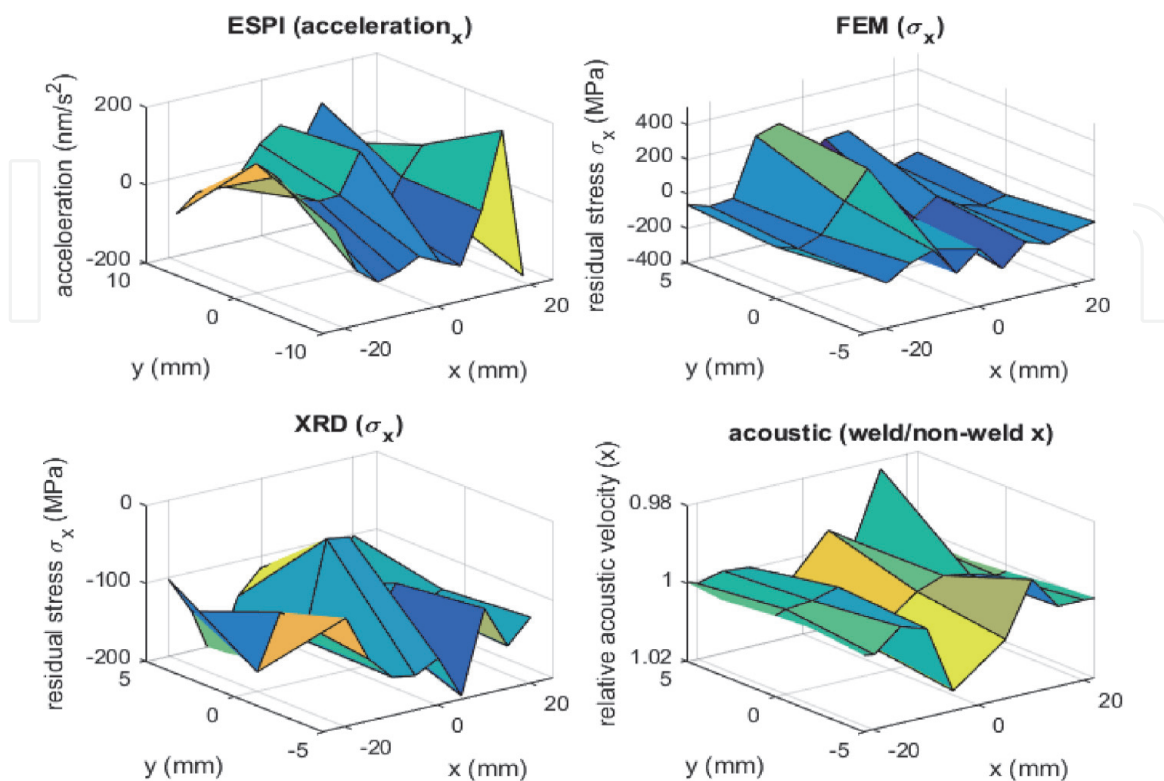
Figure 13.
*Comparison of ESPI, XRD, FEM, and acoustic results.*

the residual stress, and the acoustic result presents the relative acoustic velocity (normalized to the nominal velocity) of the x-shear wave.

Although details are different, the results from all the four analyses show qualitative agreement in the following sense. (1) All data show the general tendency that the central (near weld) region tends to have tensile residual stresses and the boundary between the central and outside regions has more compressive residual stresses. (2) Along the weld line, all data indicate that the end point of welding has higher tensile stress than the start point of welding. These observations are consistent with the following widely accepted explanation. When the welding torch heats the work, the region near the weld (the central region) is thermally expanded pushing the sides of the weld line toward the ends of the specimen (sideways). The outside regions are cooler than the central region. Consequently, the outside regions experience less thermal expansion and constrain the thermal expansion of the central region. This causes a compressive residual stress at the boundary between the central and outside regions.

In the cooling phase, the higher heat dissipation on the bottom surface locks the abovementioned stress pattern on the top surface. As the temperature of the central region goes down, the material in this region tries to shrink. However, the region behind this central region (the region closer to the bottom surface) is relatively cooler from the beginning and, therefore, does not shrink as much as the top surface. This prevents the central region near the top surface from shrinking back to the initial length. In other words, it locks tensile residual stress near the top surface.

5.1 Effect of heat dissipation

According to the above arguments, the tensile residual stress of the central region is determined by the differential rate of heat dissipation between the top and bottom surface. It is possible that increases in heat dissipation from the bottom surface (the non-welded side) can reduce this tensile stress (because it takes the heat near the top surface more aggressively). A numerical study was made to test this scenario, and the result is presented in **Figure 14**. **Figure 14a** is the case when the same convection rate is used for the top and bottom surfaces. **Figure 14b** is the case when the convection on the bottom surface is increased by a factor of two. It is seen that when the heat dissipation from the bottom surface is higher, the tendency is that the central region along the weld line is reduced. This observation confirms that in the abovementioned scenario, the heat dissipation from the bottom surface
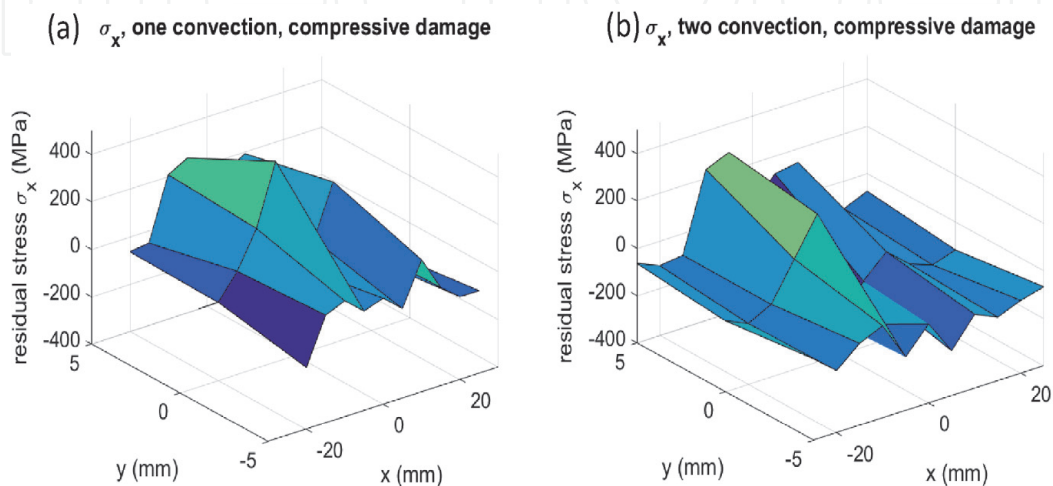
Figure 14.
Effect of heat dissipation rates. (a) The same convection is used for top and bottom surfaces; (b) convection is doubled for bottom surface.

causes the tensile residual stress on the top surface in the following sense. If the heat dissipation from the bottom surface is higher, the temperature gradient along the thickness of the specimen is lower in the cooling phase. This reduces the above-argued locking mechanism.

The case when the bottom surface has higher heat dissipation rate appears to be closer to the experimental result with ESPI shown in **Figure 13**. This is not surprising because the specimen was placed on a steel block (**Figure 12**) that behaved as a heat sink through the bottom surface. Contrastively, the top surface was exposed to air. It is reasonable to assume that the steel block was a greater heat sink than the ambient air.
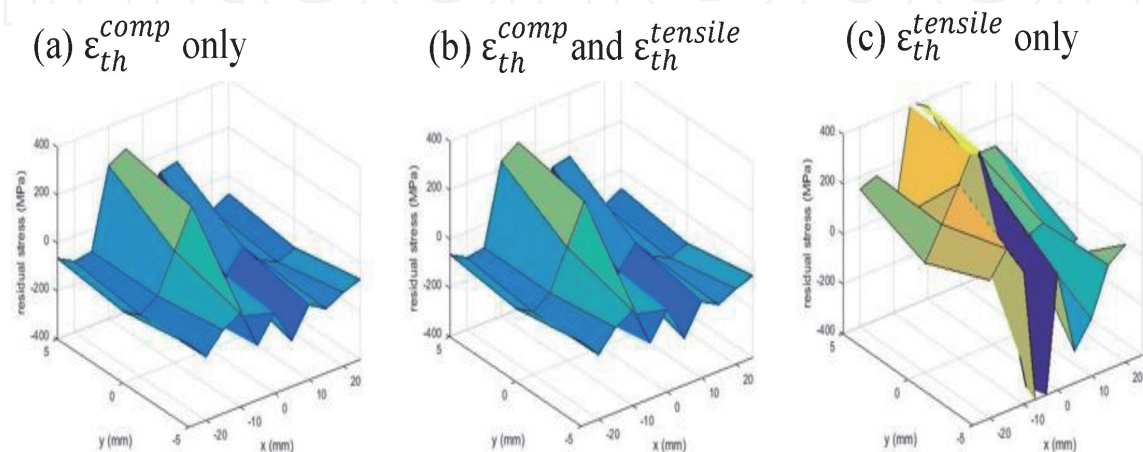
5.2 Effect of permanent strain setting

The present FEM simulates the residual stress by making the strain exceed the yield strain permanent. As discussed above, during the heating and cooling phases, both tensile and compressive residual stresses are created. This indicates that both tensile and compressive permanent strain can create residual stress, and it is a good question which type has greater contribution to the creation of residual stress. A numerical study was conducted to investigate this effect.

Figure 15 shows the x-component of residual stress on the top surface. Here the x-axis is the axis parallel to the top surface and perpendicular to the weld line. **Figure 15a–c** shows the results from the three different conditions regarding the permanent deformation setting. (a) is the case when only the compressive yield strain is used for the permanent deformation setting, (b) is the case when both of the compressive and tensile yield strains are used, and (c) is the case when the tensile yield strain only is used. The heat dissipation setting for these cases is that the bottom surface has twice as high convection than the top surface. **Figure 15a, b** shows practically no difference. On the other hand, (c) is different from (a) and (b). These altogether indicate that the effect of compressive permanent deformation plays a more important role than the effect of tensile permanent deformation in the formation of residual stresses.

5.3 Effect of TOEC

Acoustoelastic method relies on the nonlinear elasticity (the third-order elastic constant). It is interesting to compare the acoustic velocity measured for all three

(a) ε_{th}^{comp} only   (b) ε_{th}^{comp} and $\varepsilon_{th}^{tensile}$ (c) $\varepsilon_{th}^{tensile}$ only

Figure 15.
Effect of permanent deformation setting. (a) Compressive yield strain only, (b) compressive and tensile yield strain, and (c) tensile yield strain only is considered.
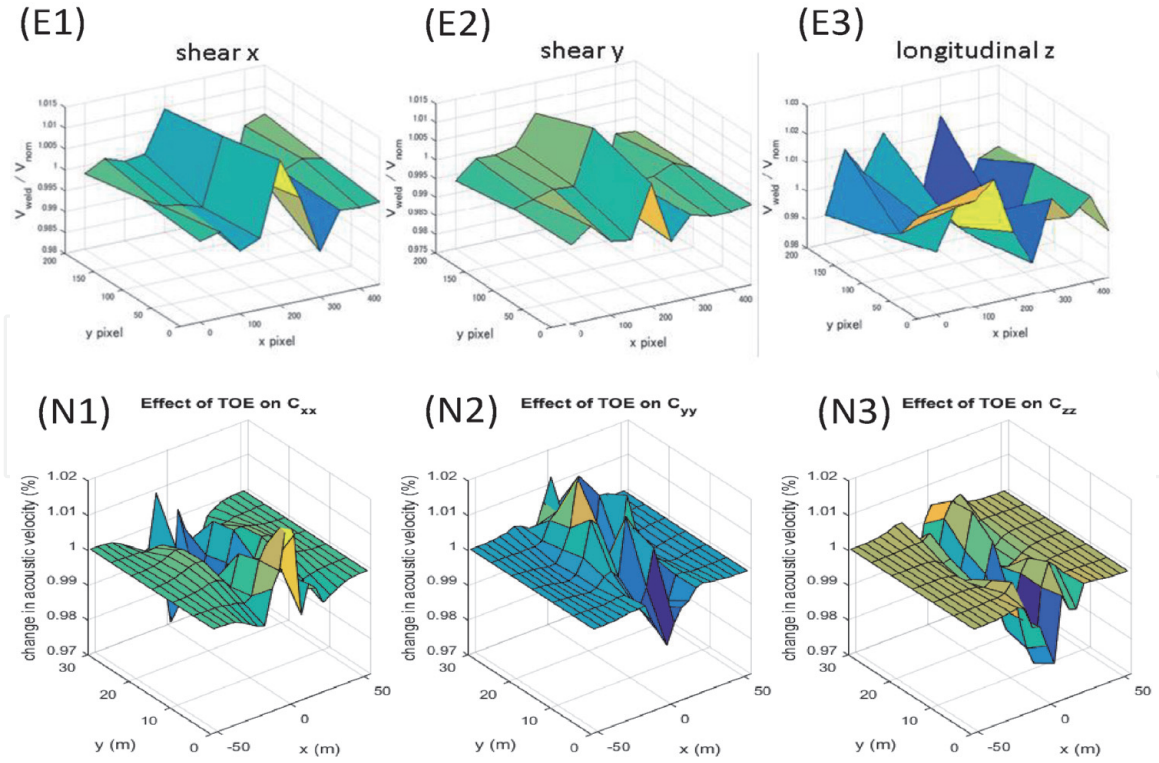
Figure 16.
Effect of TOEC based on the comparison of experimental relative acoustic velocity data. (E1)–(E3): Experimental relative velocity in x, y, and z-directions. (N1)–(N3): Numerical data corresponding to (E1)–(E3).

directions with numerical analysis conducted with the finite element model discussed above.

The top rows of **Figure 16** are the relative acoustic velocity (acoustic velocities normalized to the nominal value) measured with the contact acoustic transducer. The bottom graphs are numerical data corresponding to the three relative acoustic velocities, evaluated with the use of Eq. (22). For all three directions, the experimental and numerical results show qualitative agreement in the overall shape of the graphs. More importantly, **Figure 16** shows that the experimental and numerical changes in the acoustic velocity are in the same range, i.e., compressive/tensile residual stresses increase/decrease the acoustic velocity approximately by 1–2%. It should be noted that the root-mean-square error in the experimental acoustic velocity measured on a specimen with no residual stress is less than 0.05%.

The above agreement opens up a new way to use the conventional acoustoelastic technique. The general procedure is as follows. It is assumed that the second-order and third-order elastic coefficients (c_{ij}, c_{ijk}, etc.) are known:

Step 1: Measure the change in the acoustic velocity for all degrees of freedom, i.e., the longitudinal wave along the x (y, z) axis and the shear wave along the xy (yz, zx) surface.

Step 2: Use Eq. (22) backward to compute ΔC_{ij}.

Step 3: Use Eq. (13), etc. to find the strain vector.

Step 4: Use Eq. (11) to find the residual stress.

This procedure has not been tested yet but is a subject of our future study.

6. Summary

Applications of multiple methods to residual stress analyses are discussed. The idea behind the use of multiple methods is to compensate drawbacks of each

method. Previous experimental and numerical studies on welding-induced residual stresses are presented and discussed. These previous results show consistency among the different methods used. Further research is definitely necessary to confirm more quantitative agreement in the results obtained by the different methods. Some procedural proposals are presented as subjects of future research. It is our hope that the content of this article is helpful to engineers and researchers of the related fields.

Acknowledgements

Author details

Sanichiro Yoshida[1*] and Tomohiro Sasaki[2]

1 Department of Chemistry and Physics, Southeastern Louisiana University, Hammond, LA, USA

2 Department of Mechanical Engineering, Niigata University, Niigata, Japan

*Address all correspondence to: syoshida@selu.edu

IntechOpen

References

[1] Schajer GS, editor. Practical Residual Stress Measurement Methods. Chichester, UK: Wiley; 2013

[2] Kandil FA, Lord JD, Fry AT, Grant PV. A Review of Residual Stress Measurement Methods—A Guide to Technique Selection; NFL Report MATC(A)O4. Teddington, UK: National Physical Laboratory; 2001

[3] Schajer GS, Yang L. Residual-stress measurement in orthotropic materials using the hole-drilling method. Experimental Mechanics. 1994;**12**:324-333

[4] Eijpe MPIM, Powell PC. Determination of residual shear stress in composite by a modified layer-removal method. Journal of Materials Science. 1998;**33**:20192026

[5] Roberts SJ, McCartney LN, Broughton WR. A novel method of determining stress distribution in plates using the incremental slitting technique. Journal of Strain Analysis for Engineering Design. 2011;**46**:280-297

[6] Tebedge N, Alpsten G, Tall L. Residual-stress measurement by the sectioning method. Experimental Mechanics. 1973;**13**:88-96

[7] Drescher-Krasicka E, Willis JR. Mapping stress with ultrasound. Nature. 1996;**384**:52-55

[8] Drescher-Krasicka E, Ostertag CP. Residual stress measurements in welded steel beam columns by scanning acoustic microscopy. Journal of Materials Science. 1999;**34**:4173-4179

[9] Fitzpatrickl ME, Fry AT, Holdway P, Kandil FA, Shackleton J, Suominen L. Determination of residual stress by X-ray diffraction—Issue 2. In: Measurement Good Practice Guide. Vol. 52. Teddington, UK: National Physical Laboratory; 2005

[10] Fitzpatrick ME, Lodini A. Analysis of Residual Stress by Diffraction Using Neutron and Synchrotron Radiation. New York, USA: CRC Press; 2003

[11] Hughes DS, Kelly JL. Second-order elastic deformation of solids. Physics Review. 1953;**92**:1145-1149

[12] Duquennoy M, Ouaftouh M, Ourak M, Jenot F, Xu WJ. Theoretical and experimental determination of the natural and initial acoustoelastic coefficients. Review of Progress in Quantitative Nondestructive Evaluation. 2002;**21**:16961702

[13] Dorfi HR, Busby HR, Janssen M. Ultrasonic stress measurements based on the generalized acoustic ratio technique. International Journal of Solids and Structures. 1996;**33**:11571174

[14] Duquennoy M, Ouaftouh M, Ourak M, Jenot F. Theoretical determination of Rayleigh wave acoustioelastic coefficients: Comparison with experimental values. Ultrasonics. 2002;**39**:575583

[15] Berruti T, Gola MM, Briggs GD. Acoustoelastic measurements on aluminum alloy by means of a contact and non-contact (LFB acoustic microscopy) technique. Journal of the Acoustical Society of America. 1998;**103**: 1370-1376

[16] Lee YC, Kuo SH. A new point contact surface acoustic wave transducer for measurement of acoustoelastic effect of polymethylmethacrylate. IEEE Transactions on Ultrasonics, Ferroelectrics, and Frequency Control. 2004;**51**:114-120

[17] Muir DD. One-sided ultrasonic determination of third order elastic constants using angle-beam acoustoelasticity measurements

[PhD thesis]. Atlanta, GA, USA: Georgia Institute of Technology; 2009

[18] Vikram CS, Pechersky MJ, Feng C, Engelhaupt D. Residual-stress analysis by local laser heating and speckle-correlation interferometry. Experimental Techniques. 2008;**20**:2730

[19] Withers PJ. Depth capabilities of neutron and synchrotron diffraction strain measurement instruments. II. Practical implications. Journal of Applied Crystallography. 2004;**37**: 607-612

[20] Casavola C, Campanelli SL, Pappalettere C. Preliminary investigation on distribution of residual stress generated by the selective laser melting process. Journal of Strain Analysis for Engineering Design. 2009;**44**:93104

[21] Prevéy PS. X-ray diffraction residual stress techniques. In: Metals Handbook. Vol. 10. Metals Park: American Society for Metals; 1986. pp. 380-392

[22] Zinin PV. Quantitative acoustic microscopy of solids. In: Levy M, Bass H, Stern R, Keppens V, editors. Handbook of Elastic Properties of Solids, Liquids, and Gases. Vol. I: Dynamic Methods for Measuring the Elastic Properties of Solids. New York, USA: Academic Press; 2001. pp. 187-226

[23] Zinin PV, Arnold W, Weise W, Berezina S. Chapter 11: Theory and applications of scanning acoustic microscopy and scanning near-field acoustic imaging. In: Kundu T, editor. Ultrasonic and Electromagnetic NDE for Structure and Material Characterization: Engineering and Biomedical Applications. New York, USA: CRC Press; 2012

[24] Fuck RF, Tsvankin I. Analysis of the symmetry of a stressed medium using nonlinear elasticity. Geophysics. 2009; **74**(5):WB79-WB87

[25] Barsch GR, Chang Z. Second-and higher-order effective elastic constants of cubic crystals under hydrostatic pressure. Journal of Applied Physics. 1968;**39**:3276-3284

[26] Yoshida S, Sasaki T, Usui M, Sakamoto S, Gurney D, Park IK. Residual stress analysis based on acoustic and optical methods. Materials. 2016;**9**(2):112. DOI: 10.3390/ma9020112

[27] Yoshida S, Sasaki T, Usui M, Sakamoto S, Park I-K, Jung JH, et al. Near weld stress analysis with optical and acoustic methods. In: Bossuyt S, Schajer G, Carpenteri A, editors. Residual Stress, Thermomechanics and Infrared Imaging, Hybrid Techniques and Inverse Problems, Vol. 9, Conference Proceedings of the Society for Experimental Mechanics; 2016. pp. 119-127

[28] Graff KF. Wave Motion in Elastic Solids. New York, USA: Dover; 1975

[29] Yoshida S, Miura F, Sasaki T, Didie DR, Rouhi S. Optical analysis of residual stress with minimum invasion. In: Baldi J, Considine M, Quinn S, Balandraud X, editors. Residual Stress, Thermomechanics and Infrared Imaging, Hybrid Techniques and Inverse Problems, Vol. 8, Conference Proceedings of the Society for Experimental Mechanics; 2018. pp. 65-72

[30] Aluminum Alloys Aluminum 5083 Properties, Fabrication and Applications. Supplier Data by Aalco. Available from: http://www.azom.com/article.aspx?ArticleID=2804 [Accessed: March 13, 2019]